PAPER

Controlling the thermoelectric properties of organo-metallic coordination polymers through backbone geometry†

Zilu Liu,[a] Md Azimul Haque,[b] Chris N. Savory, [ID] [ac] Tianjun Liu, [ID] [d] Satoru Matsuishi,[ef] Oliver Fenwick, [ID] [d] David O. Scanlon, [ID] [acg] Martijn A. Zwijnenburg, [ID] [ac] Derya Baran*[b] and Bob C. Schroeder [ID] *[a]

Poly(nickel-benzene-1,2,4,5-tetrakis(thiolate)) (**Ni-btt**), an organometallic coordination polymer (OMCP) characterized by the coordination between benzene-1,2,4,5-tetrakis(thiolate) (**btt**) and Ni^{2+} ions, has been recognized as a promising p-type thermoelectric material. In this study, we employed a constitutional isomer based on benzene-1,2,3,4-tetrakis(thiolate) (**ibtt**) to generate the corresponding isomeric polymer, poly(nickel-benzene-1,2,3,4-tetrakis(thiolate)) (**Ni-ibtt**). Comparative analysis of **Ni-ibtt** and **Ni-btt** reveals several common infrared (IR) and Raman features attributed to their similar square-planar nickel–sulfur (Ni–S) coordination. Nevertheless, these two polymer isomers exhibit substantially different backbone geometries. **Ni-btt** possesses a linear backbone, whereas **Ni-ibtt** exhibits a more undulating, zig-zag-like structure. Consequently, **Ni-ibtt** demonstrates slightly higher solubility and an increased bandgap in comparison to **Ni-btt**. The most noteworthy dissimilarity, however, manifests in their thermoelectric properties. While **Ni-btt** exhibits p-type behavior, **Ni-ibtt** demonstrates n-type carrier characteristics. This intriguing divergence prompted further investigation into the influence of OMCP backbone geometry on the electronic structure and, particularly, the thermoelectric properties of these materials.

[a]*Department of Chemistry, University College London, London WC1H 0AJ, UK. E-mail: b.c.schroeder@ucl.ac.uk*

[b]*King Abdullah University of Science and Technology (KAUST), Physical Sciences and Engineering Division (PSE), KAUST Solar Center (KSC), 23955, Thuwal, Saudi Arabia. E-mail: derya.baran@kaust.edu.sa*

[c]*Thomas Young Centre, University College London, London WC1E 6BT, UK*

[d]*School of Engineering and Materials Science, Queen Mary University of London, London E1 4NS, UK*

[e]*International Center for Materials Nanoarchitectonics (WPI-MANA), National Institute for Materials Science (NIMS), 1-1 Namiki, Tsukuba, Ibaraki 305-0044, Japan*

[f]*Materials Research Center for Element Strategy, Tokyo Institute of Technology, 4259 Nagatsuta-cho, Midori-ku, Yokohama 226-8503, Japan*

[g]*Diamond Light Source Ltd., Diamond House, Harwell Science and Innovation Campus, Didcot, Oxfordshire OX11 0DE, UK*

† Electronic supplementary information (ESI) available. See DOI: https://doi.org/10.1039/d3fd00139c

Introduction

Organo-metallic coordination polymers (OMCPs) represent a fascinating class of hybrid materials that have attracted significant attention in recent years due to their unique structural and electronic properties.[1,2] These materials consist of metal cations coordinated to organic ligands, thus forming extended networks. The combination of metal ions and organic ligands allows for the design and synthesis of materials with tailored properties. Metal-tetrathiolate (MS_4) coordination systems, in particular, have garnered significant attention in recent years due to their self-assembly, high electrical conductance, metallic behaviour, porosity, and electrocatalytic activity.[3-8] In addition, the ease of synthesis facilitated by employing polyfunctionalised aromatic ligands, such as 1,4-benzenedithiol, benzenehexathiol, triphenylenehexathiol or perthiolated coronene, has led to the production of a wide range of OMCPs with intriguing thermoelectric properties.[9-12] Poly(nickel-benzene-1,2,4,5-tetrakis(thiolate)) (**Ni-btt**) stands out compared to other one-dimensional ladder-type polymers, *e.g.* poly(nickel-ethylenetetrathiolate) (**Ni-ett**), as **Ni-btt** displays p-type character, contrary to the commonly encountered n-type thermoelectric characteristics in Ni-based OMCPs.[13]

To optimise the thermoelectric properties of OMCPs further, significant efforts have been dedicated to material synthesis, batch-to-batch reproducibility, morphology control, and processability.[13-17] The primary focus was put on the synthetic conditions by exploring different transition-metal centres, adjusting the ligand-to-metal ratios, controlling oxidation levels, and utilising electrochemical synthesis. Additionally, different processing approaches, such as ball-milling, blending with polymer binders, and thermal annealing, have enabled the successful fabrication of OMCP films and their incorporation into thermoelectric generators.[17-19]

To gain further insights into the electronic structures and physical properties of the poly(M-ett) family and its derivatives, density functional theory (DFT) calculations have proven instrumental.[20-23] DFT calculations have facilitated the understanding of structure–property relationships and provided a basis for initial molecular design considerations by exploring different combinations of metal centres and organic ligands. Despite these advancements, the number of structurally novel OMCPs remains limited, and significant synthetic efforts are necessary to experimentally determine their potential structure–property relationships. In a recent study, we reported the thermoelectric performance of two novel linear π–d conjugated organometallic coordination polymers: poly(nickel-[2,2′-bi(1,3-dithiolylidene)]4,4′,5,5′-tetrakis(thiolate)) (**Ni-diett**) and poly(nickel-benzene-1,2,4,5-tetrakis(thiolate)) (**Ni-btt**), along with **Ni-ett**.[13]

Efforts to enhance the processability of organometallic coordination polymers (OMCPs) have become a significant focus of interest. One potential strategy to achieve this goal involves reducing molecular order through ligand design, which can render the polymer more soluble. In this study, we address this objective by synthesising a structural isomer of the btt ligand, namely benzene-1,2,3,4-tetrakis(thiolate) (**ibtt**). The ibtt ligand differs from the previously studied D_{2h}-symmetric btt ligand in its C_{2v} symmetry and as such should reduce molecular order and thereby enhance solubility. Our study encompasses the preparation,

structural characterization, and thermoelectric measurements of the OMCPs incorporating these two isomeric ligands, focusing on MS_4 complexes with high structural integrity and a square-planar coordination.

In contrast to the previously reported p-type behaviour of **Ni-btt**, our investigations reveal that **Ni-ibtt** exhibits n-type characteristics. It displayed a moderate electrical conductivity (σ) on the order of 10^{-2} S cm^{-1} and an encouraging Seebeck coefficient (-60 μV K^{-1}). Spectroscopic characterization techniques, including UV-visible, FTIR, and Raman spectroscopy, were employed to analyse **Ni-ibtt** and **Ni-btt**, as well as a series of intermediate compositions, **Ni(ibtt)$_x$(btt)$_{1-x}$**, to gain a deeper understanding of the underlying structure–property relationships.

Our work unveils the profound impact that modest structural differences in the organic ligands can have on the overall thermoelectric properties of the resulting OMCPs. Through a combination of experimental characterization and theoretical simulations, we provide valuable insights into the tuning of thermoelectric properties by altering the ratio of ligand isomers. Additionally, this work reports the synthesis of a metal-ibtt coordination polymer and its corresponding thermoelectric performance. Overall, our findings contribute to a deeper understanding of the relationship between organic ligand structure and thermoelectric properties in OMCPs.

Results and discussion

Synthesis

The synthesis of 1,2,4,5-tetrakis(isopropylthio)benzene (TIB) as a precursor for the preparation of **Ni-btt** [**btt** = benzene-1,2,4,5-tetrakis(thiolate)] followed the same method as described in our previous report.[13] The synthesis of **Ni-ibtt** and **Ni(ibtt)$_x$(btt)$_{1-x}$** was conducted using a slightly adapted procedure, employing 1,2,3,4-tetrakis(isopropylthio)benzene (iTIB) as the OMCP precursor ligand. The detailed synthetic procedures are provided in the ESI† and the chemical structures of the various OMCPs are depicted in Fig. 1. The different samples were purified *via* Soxhlet extraction, washing the crude OMCP with deionized water and methanol for 24 hours each.

Compositional and structural characterisation

To analyse the chemical composition of the new **Ni-ibtt**, X-ray photoelectron spectroscopy (XPS) was conducted (Fig. 2 and S5†) and the data compared to the previously characterised **Ni-btt**. The survey spectra confirmed the presence of Ni, S, and C as the primary constituent elements (other than hydrogen, which our XPS
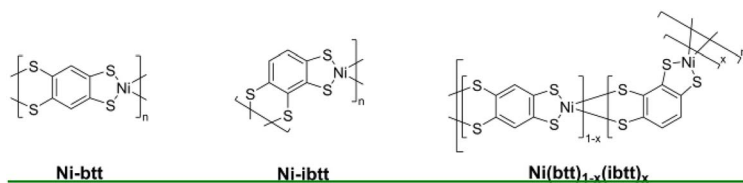

Ni-btt   **Ni-ibtt**   **Ni(btt)$_{1-x}$(ibtt)$_x$**

Fig. 1 Chemical structures of the OMCPs incorporating different ligand isomers.
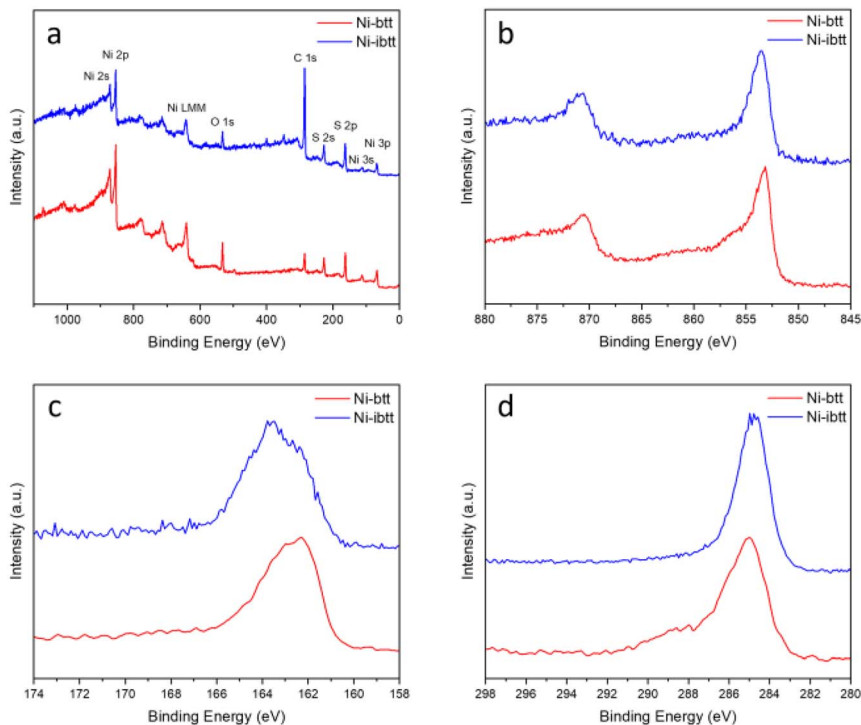
Fig. 2 XPS spectra of **Ni-btt** and **Ni-ibtt**: (a) survey scan, (b) Ni 2p, (c) S 2p and (d) C 1s.

system cannot detect). The Ni 2p photoemission spectrum of **Ni-ibtt** exhibited two peaks at binding energies of 853 and 873 eV, corresponding to the Ni $2p_{3/2}$ and Ni $2p_{1/2}$ spin–orbit splitting, respectively. These observations indicate the presence of a single type of Ni^{2+} species as the central metal. The S 2p XPS narrow-range scan with fitting reveals peaks at binding energies of 161.8 and 163 eV, which were attributed to Ni-thiolate complexation. In line with previous observations, neither the XPS energy survey spectrum, nor the Na 1s core level XPS spectrum (Fig. S6†) provided any evidence for the presence of residual Na from the synthesis, thus ruling out the possibility of excess Na acting as a counter anion in the **Ni-ibtt** OMCP.

To further assess the chemical composition, X-ray fluorescence (XRF) analysis was performed (Table S1†). The experimental S/Ni ratio determined by XRF for **Ni-ibtt** was 3.15, reasonably close to the theoretical S/Ni ratio of 4. We believe that the discrepancy between experimental and theoretical values can be explained by the poor solubility of **Ni-ibtt** and the challenging purification on the one hand, and by the likely presence of structural defects along the polymer backbones affecting the ratio on the other hand. Besides the S/Ni ratio, however, it is noteworthy that the XRF data confirmed the absence of any significant additional elements, Na or others, acting as potential counter cations in the **Ni-ibtt** sample, thus providing further evidence for the charge-neutral character of the polymer backbone. Prior studies on structurally similar MS_4 and $M(NH)_4$-based OMCPs described the presence of charge-neutral radicals and Raman

spectroscopy experiments were performed to elucidate the distinct Raman signature of thiocarbonyl radicals (C=S˙).[24]

Attenuated total reflection Fourier transform infrared (ATR-FTIR) and resonance Raman spectroscopy were conducted on the organic ligands TIB and iTIB (Fig. S8†) and compared to the data collected for the corresponding OMCPs. In the FTIR spectrum of **Ni-ibtt** (Fig. 3a), the distinct C=S˙ stretching vibration modes were observed at 1133 cm^{-1}, along with a split peak at 1071–1012 cm^{-1}. The higher wavenumber range (1596–1398 cm^{-1}) was attributed to the aromatic semicircular stretching and the ring quadrant stretching mode.

The Raman spectrum of **Ni-ibtt** exhibited several striking similarities to the **Ni-btt** spectrum, primarily due to the structural resemblance between the ibtt and btt ligands and the corresponding MS$_4$ coordination bonds formed (Fig. 3b). The characteristic vibration mode at 357 cm^{-1} observed for both **Ni-btt** and **Ni-ibtt** is attributed to Ni–S coordination. Notably, **Ni-ibtt** displays a less intense peak from ν(Ni–S) compared to the series of aromatic peaks in the Raman spectrum, in contrast to **Ni-btt**. Considering the isomeric ligand, the presence of four adjacent C–S bonds in ibtt distorts the electric charge separation, resulting in a higher intrinsic dipole moment ($\mu = q \times d$, where q is the charge and d is the distance) with deviation from the centre of the benzene ring, in comparison to btt. Consequently, the coordination in **Ni-ibtt** leads to a considerable charge separation, with the positive charge located on the Ni atom while the negative charge is delocalized over the organic ligand. Raman vibrational modes originating from highly polar moieties typically exhibit weaker intensities. In other words, the external electric field cannot induce a notable change in the dipole moment of Ni–S in **Ni-ibtt** compared to **Ni-btt**, hence the ν(Ni–S) peak is weaker in intensity.

The Raman spectra of both organic ligands, TIB and iTIB (Fig. S9†), differ slightly in the signals arising from their respective out-of-plane C–H bending vibrations (<1000 cm^{-1}). These vibrations, however, were not observable in the Raman spectra of the two OMCPs and appeared in the FTIR spectra instead at 870 cm^{-1} for **Ni-ibtt**, with a stronger band at 857 cm^{-1} in the case of **Ni-btt**. The sharp peak at 1095 cm^{-1} observed in the Raman spectrum of **Ni-ibtt** is attributed to the ν(C=S˙) stretching vibration of the ligand, accompanied by a weaker, adjacent peak at 1141 cm^{-1}.
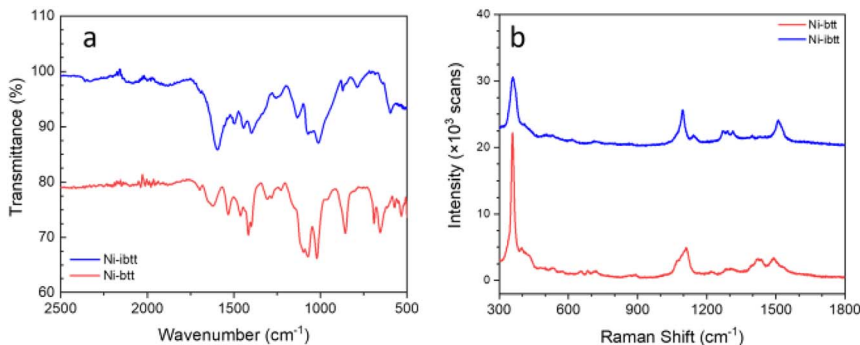

Fig. 3 FTIR (a) and resonance Raman (728 nm excitation) (b) spectra of **Ni-btt** and **Ni-ibtt** after purification. The spectra have been stacked for clarity.

Polymer backbone geometry and solid-state packing

After confirming the chemical composition of the novel **Ni-ibtt**, our focus shifted towards differences in the 'shape' of the polymers and their solid-state packing. Based on previous observations in the field of organic semiconducting polymers,[25,26] the assumption was that the ibtt ligand with its C_{2v} symmetry would disrupt the polymer packing in the solid state and hence increase the solubility and processability of the resulting **Ni-ibtt** compared to **Ni-btt**. To investigate the effect of symmetry on OMCP backbone geometry, density functional theory (DFT) calculations were conducted on oligomeric models of **Ni-btt** and **Ni-ibtt**, discussed in more detail below, and the optimised molecular geometries are shown in Fig. 4.

Like **Ni-btt**, the Ni atoms in **Ni-ibtt** participate in the formation of square-planar complexes with the iTIB ligand. Due to the higher symmetry of the TIB ligand, the resulting **Ni-btt** OMCP has a linear polymer backbone. In **Ni-ibtt**, however, the lower C_{2v} symmetry of the organic ligand allows for the formation of either *cis*- or *trans*-configurations along the polymer backbone, leading to a wavy or zig-zagged backbone (Fig. 4). To facilitate the DFT calculations, we assumed a 100% *trans*-arrangement in **Ni-ibtt**. During the synthesis, however, no efforts were made to control the orientation of the organic ligands relative to each other, and it should be assumed that their arrangement is random in the synthesised **Ni-ibtt**. Despite this increased disorder along the polymer backbone, the planar geometry of the NiS_4 complex ensures that the overall planarity of the OMCP is not affected. In the unlikely event that all metal–ligand complexes would arrange in a *cis*-configuration in the **Ni-ibtt**, it would be possible for the chain ends to link up and form a cyclic oligomer (Fig. S13†). While the formation of cyclic oligomers comprising $[Ni_6L_6]$ is conceptually possible, no experimental evidence confirming their existence was found, and we will therefore disregard this molecular arrangement from the discussion.

To assess the crystallinity of the OMCP based on the isomeric ligands, powder X-ray diffraction (XRD) spectra were recorded for both materials. In comparison to the linear **Ni-btt**, **Ni-ibtt** exhibited two broad peaks at 5.9° and 12.1° that were similar in position to the peaks in the former. However, an additional peak at 3.8° was observed in **Ni-ibtt**, indicating a wider *d*-spacing of 10.7 Å, resulting from its wavy and less ordered backbone (Fig. S14†).

Thermoelectric characterization

Before studying the thermoelectric properties of **Ni-ibtt**, it was important to evaluate its thermal stability through thermogravimetric analysis (TGA)
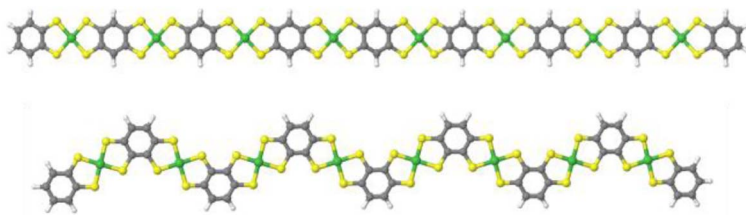

Fig. 4 Minimum energy conformations obtained from DFT calculations for octamers of **Ni-btt** (top) and **Ni-ibtt** (bottom) with all metal–ligand complexes in *trans*-configuration.

(Fig. S15†). In comparison to **Ni-btt**, **Ni-ibtt** exhibited a lower thermal stability and gradually started degrading from 150 °C onwards. Moreover, the degradation of **Ni-ibtt** was slower compared to **Ni-btt**, which displayed a sharp weight loss at approximately 300 °C. Despite the decomposition temperature of **Ni-ibtt** being relatively elevated, thermal annealing of a **Ni-ibtt** pellet at 150 °C, under ambient conditions, led to partial surface oxidation as evidenced by XPS measurements (Fig. S7†). The S 2p peak at 168 eV is representative of sulfate contaminants in the sample. Notably, the oxidation was limited to the surface, and after sputtering 15 nm beneath the surface, the XPS spectrum revealed again a pristine S 2p peak without any discernible change indicative of oxidation.

Intrinsically air-stable n-type organic thermoelectric materials are scarce, and while many OMCPs previously demonstrated n-type behaviour, **Ni-btt** was one of the first materials to show p-type behaviour instead, as a consequence of the chemical structure of the ligand. Considering that **Ni-ibtt** is a constitutional isomer of **Ni-btt**, we were expecting the OMCP to display p-type thermoelectric characteristics. The thermoelectric properties of **Ni-ibtt** are depicted in Fig. 5, demonstrating, contrary to our hypothesis, that **Ni-ibtt** is another air-stable n-type OMCP with a negative Seebeck coefficient, similar to the widely reported **Ni-ett**.

Ni-ibtt exhibited a relatively stable Seebeck coefficient of around $-60\ \mu V\ K^{-1}$ in the studied temperature range. The profound effect of organic ligand isomerism on the nature of transported charges was unexpected. To date only one report explored **Ni-ibtt** in an all-trans conformation for its thermoelectric potential, relying on DFT calculations.[23] The thermoelectric properties were computed both for p- and n-type performance, yet no conclusion with regards to the Seebeck was drawn. However, it was stated that the orbital conjugation between the sulfur atoms in the para-positions and the bridging C–C bonds would be the only hole-conducting channel and that therefore **Ni-ibtt** would be "detrimental for hole transport",[23] a finding that is consistent with our observation of n-type behaviour in **Ni-ibtt** and which could explain why **Ni-btt** and **Ni-ibtt** display opposing behaviour.

To gain a deeper understanding of the electronic structure of the isomeric OMCPs, DFT calculations were performed on both finite cluster (oligomers) and periodic (infinitely repeating chains) models of isolated **Ni-btt** and **Ni-ibtt**
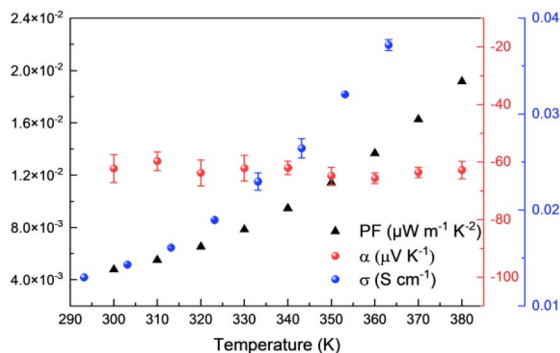

Fig. 5 Thermoelectric properties of **Ni-ibtt**: electrical conductivities (blue dots), Seebeck coefficients (red dots) and power factors (black triangles).

polymers. The cluster DFT calculations, using the hybrid B3LYP functional,[27–30] on the tetrameric oligomeric models of **Ni-btt** and **Ni-ibtt** (see Fig. S19†) predict that while the electronic ground state of **Ni-btt** is a spin-polarised open-shell singlet, the electronic ground state of **Ni-ibtt** is a closed-shell singlet. Similarly, in the periodic DFT calculations, which use the hybrid HSE06 functional,[31,32] the ground-state configuration of **Ni-btt** was found to be an open-shell singlet and that of **Ni-ibtt** a closed-shell singlet. The predicted closed-shell character of **Ni-ibtt** was experimentally confirmed by electron paramagnetic resonance (EPR) and superconducting quantum interference device (SQUID) measurements (Fig. S16 to S18†). In the EPR spectra, two main types of signals were observed: a broad low-field signal and a narrow central-field signal. The former can be identified as a high-spin (triplet) state of Ni^{2+}, whereas the latter originates from a low spin Ni^{3+}. However, the concentration of unpaired electrons is very low, indicating that **Ni-ibtt** is intrinsically nonmagnetic with a low spin state of Ni^{2+} ($S = 0$).

When visualising the highest occupied and lowest unoccupied molecular orbitals (HOMO and LUMO) of the **Ni-ibtt** tetramer (see Fig. S20),† there is evidence of "cross-conjugation". The contribution of the atomic orbitals of the two sulfur atoms along one diagonal of the NiS_4 coordination environments is larger than that of the sulfur atoms along the other diagonal. In contrast, the contribution of the sulfur atoms around the nickel cations in **Ni-btt** to the highest singly occupied and lowest singly unoccupied orbitals (SHOMO/SLUMO) is much more symmetric. The difference is that in btt each sulfur atom of the ligand coordinating a nickel cation on one side of the ligand is always para with respect to a sulfur atom of the same ligand coordinating another nickel cation, while in ibtt they are a combination of *ortho*, *meta* and *para*. The calculations on the oligomers, finally, also suggest that **Ni-btt** has a deeper lowest unoccupied orbital/more positive electron affinity than **Ni-ibtt**, and hence would be easier to reduce and n-dope than **Ni-ibtt**, while both materials are predicted to have similar HOMO/SHOMO and ionisation potential values, and hence should be comparably easy to p-dope.

The band structures predicted for infinite **Ni-btt** and **Ni-ibtt** polymers in the periodic calculations are plotted in Fig. 6. The electronic structures of both coordination polymers showed them to be narrow-gap semiconductors, with gaps of 0.47 eV for **Ni-btt** and 0.88 eV for **Ni-ibtt**; the wider gap of **Ni-ibtt** likely results from the narrower bandwidths of both conduction and valence bands. In both electronic structures, in accordance with the modelled cells preventing inter-chain interactions, band dispersion is only seen along reciprocal lines corresponding to the polymer chain direction (*e.g.* Γ to Z for **Ni-btt** and Γ to X for **Ni-ibtt**). In **Ni-btt**, the conduction band is highly disperse in both spin channels – using a parabolic fit to the band edge gives an effective mass of 0.11 m_0 (units of electron rest mass). The valence band shows significant dependence on the spin channel, with a heavy hole state in the spin up, but high local curvature at the valence band maximum in the spin down – the hole effective mass at the band edge is 0.16 m_0, comparable with the conduction band, and consistent with the high p-type conductivities observed. By comparison, both conduction and valence bands of **Ni-ibtt** show weaker dispersion than those of **Ni-btt**, in line with the cross conjugation observed in the oligomeric calculations, and higher effective masses of 0.42 m_0 and 0.70 m_0, respectively. In all, the partial cross-conjugation in the all-*trans* **Ni-ibtt** (as seen in the partial charge density in ESI Fig. S21,† and as
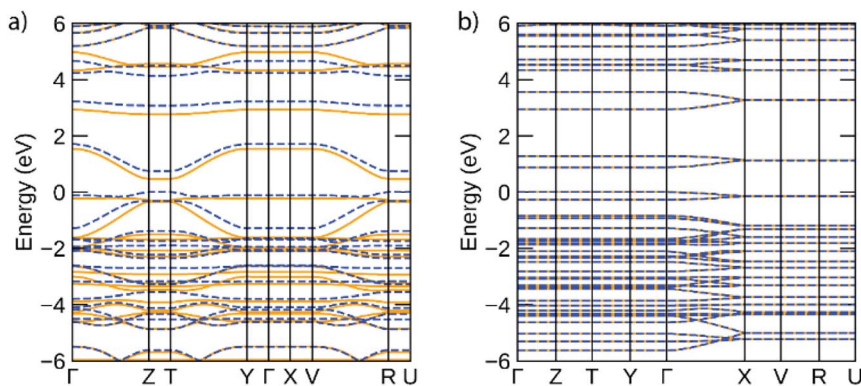
Fig. 6 Electronic band structures of (a) **Ni-btt** and (b) 100%-*trans* **Ni-ibtt**, calculated using the HSE06 functional. Spin-up bands are depicted by solid orange lines, spin-down by dashed blue lines, and the valence band maximum is set to 0 eV. This figure was plotted using the sumo package.[33]

discussed also observed in the oligomeric calculations) impacts band dispersion in comparison with the wholly linear **Ni-btt**, and appears to lead to weaker conductivities, but higher Seebeck coefficient in that system.

As discussed above, the results of the calculations suggest, in contrast to experiment, that **Ni-btt** should behave as n-type and **Ni-ibtt** as p-type, other than perhaps the prediction of the significantly lower effective mass of electrons in the conduction band than holes in the valence band for **Ni-ibtt**, which should make the former considerably more mobile than the latter, if present. It is important, however, to remember that these calculations are for the intrinsic materials and do not consider the effect of defects in the materials and how these might result in (self-)doping. The defect chemistry of these materials, be it intrinsic or extrinsic, as the result of ppm/ppb-level impurities present from synthesis, is poorly understood and likely the p-type character of **Ni-btt** and the n-type character of **Ni-ibtt** find their origin in differences in their defect chemistry.

Further differences between the two OMCPs were observed in their respective electric conductivities. Similar to **Ni-btt**, **Ni-ibtt** displayed thermally activated transport, gradually increasing from 1.4×10^{-2} S cm^{-1} at 303 K to 3.7×10^{-2} S cm^{-1} at 363 K. It is noteworthy, however, that the measured electrical conductivities are two orders of magnitude lower in **Ni-ibtt** compared to **Ni-btt**. The electrical conductivity of a coordination polymer depends on numerous factors, such as the extent of conjugation length, intra- and intermolecular orbital overlap, and overall crystallinity or molecular order of the OMCP. The most striking difference between the two materials is their molecular structure and how the **Ni-ibtt** polymer was designed with the aim to disrupt molecular packing. Whilst the XRD provided some evidence for increased *d*-spacing and molecular disruption, the lower electrical conductivities are most likely a direct consequence of poorer molecular order and reduced interchain π-stacking in the zig-zagged **Ni-ibtt**, compared to the linear **Ni-btt**. Another contributor to the lower observed mobility could be the presence of structural defects in **Ni-ibtt**, which has been demonstrated in the past to be detrimental to electrical properties.[34] As outlined

Table 1 Thermoelectric properties of **Ni-btt**, **Ni-ibtt** and **Ni(ibtt)$_x$(btt)$_{1-x}$** at 310 K

Sample	σ (S cm^{-1})	α (μV K^{-1})	PF (μW m^{-1} K^{-2})
Ni-ibtt	1.61×10^{-2}	-59.7	5.11×10^{-3}
Ni(ibtt)0.5(btt)0.5	2.54×10^{-3}	12.8	4.24×10^{-5}
Ni(ibtt)0.2(btt)0.8	1.21×10^{-1}	17.2	3.52×10^{-3}
Ni-btt	7.11	12.7	1.20×10^{-1}

earlier, partial oxidation of the sulfur in the OMCP backbone cannot be excluded and could introduce additional chemical defect sites, impeding efficient charge transport.

To investigate the effect of the isomeric ligands on the thermoelectric properties further, we synthesised two intermediate OMCP compositions, **Ni(ibtt)$_{0.5}$(btt)$_{0.5}$** and **Ni(ibtt)$_{0.2}$(btt)$_{0.8}$**. The detailed synthetic procedures and full material characterisation are provided in the ESI.† The thermoelectric properties of all four OMCP materials are summarised in Table 1. Of all four materials, **Ni(ibtt)$_{0.5}$(btt)$_{0.5}$** should experience the largest interchain disorder as the introduction of the more linear btt ligand will prevent any longer-range order in the polymer, due to the geometry mismatch between the two isomeric ligands. This assumption is supported by the much lower electrical conductivity recorded for **Ni(ibtt)$_{0.5}$(btt)$_{0.5}$**. As the interchain order is increased by introducing more btt, the electrical conductivity increases by two orders of magnitude for **Ni(ibtt)$_{0.2}$(btt)$_{0.8}$**, approaching the conductivity of **Ni-btt**. The most striking impact of ligand mixing in the OMCP however was seen on the Seebeck coefficient. Neither of the two mixed-ligand OMCPs displayed n-type characteristics, which was reserved to **Ni-ibtt**. For both **Ni(ibtt)$_{0.5}$(btt)$_{0.5}$** and **Ni(ibtt)$_{0.2}$(btt)$_{0.8}$**, the measured Seebeck coefficients were positive and of a similar magnitude as for **Ni-btt**, highlighting the importance of carefully considering the ligand composition in these OMCPs. As outlined previously, **Ni-ibtt** is a poor hole-transporting material and therefore the introduction of a good hole-transporting material, like the linear btt ligand, was expected to have a tremendous impact on the mixed OMCP transport properties.

Conclusions

In conclusion, we have synthesized a series of one-dimensional OMCPs with varying degrees of backbone linearity by introducing different constitutional isomers into the polymer backbone. The difference in bridging ligands gave rise to **Ni-ibtt**, with a more disordered zig-zagged backbone, and **Ni-btt** with a rigid and linear geometry. Through careful characterisation we were able to determine the chemical composition of both isomeric organometallic coordination polymers and confirm the charge-neutral character of the polymer backbone. When assessing the thermoelectric properties of the novel OMCPs, we found that the wavy, less ordered backbone of **Ni-ibtt** yielded a much lower electrical conductivity (1.61×10^{-2}), while at the same time displaying a negative Seebeck coefficient (-59.7 μV K^{-1}). By moderating the ratio of btt/ibtt ligands in the OMCPs and subsequently the backbone geometry and molecular order in the materials, we were able to gain control over the thermoelectric properties and moderate both

the charge transport and the thermovoltage. To the best of our knowledge, this is the first experimental demonstration of the profound impact of OMCP backbone geometry on thermoelectric properties, thus highlighting the complexity of various structural factors to consider when designing and optimizing new thermoelectric OMCPs.

Author contributions

ZL and BCS contributed to conception, design, data acquisition (synthesis, FTIR, Raman, UV-vis, TE characterisation). MAH, TL, OF and DB recorded the thermoelectric properties. CNS, DOS and MAZ performed the DFT calculations. SM conducted the SQUID and EPR measurements. All authors contributed to data analysis, drafted, and critically revised the article. All authors gave their final approval and agree be accountable for all aspects of the work.

Conflicts of interest

There are no conflicts to declare.

Acknowledgements

References

1 H. Liu, Y. Wang, Z. Qin, D. Liu, H. Xu, H. Dong and W. Hu, *J. Phys. Chem. Lett.*, 2021, **12**, 1612–1630.

2 G. H. Morritt, H. Michaels and M. Freitag, *Chem. Phys. Rev.*, 2022, **3**, 011306.

3 C. A. Downes and S. C. Marinescu, *J. Am. Chem. Soc.*, 2015, **137**, 13740–13743.

4 C. Hu, Q. Ma, S.-F. Hung, Z.-N. Chen, D. Ou, B. Ren, H. M. Chen, G. Fu and N. Zheng, *Chem*, 2017, **3**, 122–133.

5 X. Huang, S. Zhang, L. Liu, L. Yu, G. Chen, W. Xu and D. Zhu, *Angew Chem. Int. Ed. Engl.*, 2018, **57**, 146–150.

6 R. Dong, P. Han, H. Arora, M. Ballabio, M. Karakus, Z. Zhang, C. Shekhar, P. Adler, P. S. Petkov, A. Erbe, S. C. B. Mannsfeld, C. Felser, T. Heine, M. Bonn, X. Feng and E. Canovas, *Nat. Mater.*, 2018, **17**, 1027–1032.

7 R. Dong, Z. Zhang, D. C. Tranca, S. Zhou, M. Wang, P. Adler, Z. Liao, F. Liu, Y. Sun, W. Shi, Z. Zhang, E. Zschech, S. C. B. Mannsfeld, C. Felser and X. Feng, *Nat. Commun.*, 2018, **9**, 2637.

8 S. H. Liu, Y. C. Wang, C. M. Chang, T. Yasuda, N. Fukui, H. Maeda, P. Long, K. Nakazato, W. B. Jian, W. F. Xie, K. Tsukagoshi and H. Nishihara, *Nanoscale*, 2020, **12**, 6983–6990.

9 Y. Sun, P. Sheng, C. Di, F. Jiao, W. Xu, D. Qiu and D. Zhu, *Adv. Mater.*, 2012, **24**, 932–937.

10 R. Tkachov, L. Stepien, A. Roch, H. Komber, F. Hennersdorf, J. J. Weigand, I. Bauer, A. Kiriy and C. Leyens, *Tetrahedron*, 2017, **73**, 2250–2254.

11 A. K. Menon, R. M. W. Wolfe, S. Kommandur and S. K. Yee, *Adv. Electron. Mater.*, 2019, **5**, 1800884.

12 Z. Liu, T. Liu, C. N. Savory, J. P. Jurado, J. S. Reparaz, J. Li, L. Pan, C. F. J. Faul, I. P. Parkin, G. Sankar, S. Matsuishi, M. Campoy-Quiles, D. O. Scanlon, M. A. Zwijnenburg, O. Fenwick and B. C. Schroeder, *Adv. Funct. Mater.*, 2020, **30**, 2003106.

13 C. Faulmann, J. Chahine, K. Jacob, Y. Coppel, L. Valade and D. de Caro, *J. Nanopart. Res.*, 2013, **15**, 1586.

14 P. Sheng, Y. Sun, F. Jiao, C. Liu, W. Xu and D. Zhu, *Synth. Met.*, 2014, **188**, 111–115.

15 Y. Sun, L. Qiu, L. Tang, H. Geng, H. Wang, F. Zhang, D. Huang, W. Xu, P. Yue, Y. S. Guan, F. Jiao, Y. Sun, D. Tang, C. A. Di, Y. Yi and D. Zhu, *Adv. Mater.*, 2016, **28**, 3351–3358.

16 Y. Sun, J. Zhang, L. Liu, Y. Qin, Y. Sun, W. Xu and D. Zhu, *Sci. China: Chem.*, 2016, **59**, 1323–1329.

17 A. K. Menon, R. M. W. Wolfe, S. R. Marder, J. R. Reynolds and S. K. Yee, *Adv. Funct. Mater.*, 2018, **28**, 1801620.

18 R. M. W. Wolfe, A. K. Menon, T. R. Fletcher, S. R. Marder, J. R. Reynolds and S. K. Yee, *Adv. Funct. Mater.*, 2018, **28**, 1803275.

19 W. Jin, L. Liu, T. Yang, H. Shen, J. Zhu, W. Xu, S. Li, Q. Li, L. Chi, C. A. Di and D. Zhu, *Nat. Commun.*, 2018, **9**, 3586.

20 W. Shi, G. Wu, K. Hippalgaonkar, J. S. Wang, J. Xu and S. W. Yang, *J. Am. Chem. Soc.*, 2018, **140**, 13200–13204.

21 W. Shi, G. Wu, X. Yong, T. Deng, J. S. Wang, J. C. Zheng, J. Xu, M. B. Sullivan and S. W. Yang, *ACS Appl. Mater. Interfaces*, 2018, **10**, 35306–35315.

22 M. Wu, Z. Wang, J. Liu, W. Li, H. Fu, L. Sun, X. Liu, M. Pan, H. Weng, M. Dincă, L. Fu and J. Li, *2D Materials*, 2016, **4**, 015015.

23 X. Yong, W. Shi, G. Wu, S. S. Goh, S. Bai, J.-W. Xu, J.-S. Wang and S.-W. Yang, *J. Mater. Chem. A*, 2018, **6**, 19757–19766.

24 K. Ray, T. Weyhermüller, F. Neese and K. Wieghardt, *Inorg. Chem.*, 2005, **44**, 5345–5360.

25 R. Rieger, D. Beckmann, A. Mavrinskiy, M. Kastler and K. Müllen, *Chem. Mater.*, 2010, **22**, 5314–5318.

26 B. Ding, G. Kim, Y. Kim, F. D. Eisner, E. Gutiérrez-Fernández, J. Martín, M.-H. Yoon and M. Heeney, *Angew. Chem., Int. Ed.*, 2021, **60**, 19679–19684.

27 A. D. Becke, *J. Chem. Phys.*, 1993, **98**, 5648–5652.

28 C. Lee, W. Yang and R. G. Parr, *Phys. Rev. B: Condens. Matter*, 1988, **37**, 785–789.

29 S. H. Vosko, L. Wilk and M. Nusair, *Can. J. Phys.*, 1980, **58**, 1200–1211.

30 P. J. Stephens, F. J. Devlin, C. F. Chabalowski and M. J. Frisch, *J. Phys. Chem.*, 1994, **98**, 11623–11627.

31 A. V. Krukau, O. A. Vydrov, A. F. Izmaylov and G. E. Scuseria, *J. Chem. Phys.*, 2006, **125**, 224106.

32 J. Heyd, G. E. Scuseria and M. Ernzerhof, *J. Chem. Phys.*, 2003, **118**, 8207–8215.

33 A. M Ganose, A. J Jackson and D. O Scanlon, *J. Open Source Softw.*, 2018, **3**, 717.

34 S. Dutta, S. Chakraborty, M. G. B. Drew, A. Frontera and A. Ghosh, *Cryst. Growth Des.*, 2019, **19**, 5819–5828.